Catalysis Science & Technology

ROYAL SOCIETY OF CHEMISTRY

PAPER

Cite this: *Catal. Sci. Technol.*, 2023, 13, 4367

Synthesis of new graphene oxide/TiO_2 and TiO_2/SiO_2 nanocomposites and their evaluation as photocatalysts†

Marta Rosenthal,[ac] Timur Biktagirov,[b] Wolf Gero Schmidt[b] and René Wilhelm*[c]

Received 4th April 2023,
Accepted 3rd June 2023

DOI: 10.1039/d3cy00461a

rsc.li/catalysis

This article discusses the synthesis and characterization of various composites of graphene oxide with P-25 and TiO_2/SiO_2 hybrid materials, as well as their photocatalytic behavior. Different synthetic routes to these composites were studied, including treatment with heat (300–500 °C) in a tube furnace and mechanical treatment with ultrasound. Two different types of graphene oxide were used: edge-functionalized graphene oxide (edge-GO) and graphene oxide produced using the Hummers method (Hum-GO). The photocatalytic activity of the different nanocomposites was analyzed by studying the degradation of methyl orange (MO) and the photocatalytic reduction of benzaldehyde. The influence of the different graphene oxide types, TiO_2 materials, and synthetic routes on the photocatalytic activity will be presented.

1. Introduction

In recent years, an important research goal has been the development of optimized systems for using renewable and clean energy resources.[1] Semiconductors are crucial for converting solar energy into usable energy, with TiO_2 being the most commonly applied. This is due to its specific physical and chemical properties, which make it suitable for use in solar cells, dye systems, and electrochemical systems.[2] TiO_2 is advantageous because it has long-term thermodynamic stability, is non-toxic, has low commercial acquisition costs, and exhibits wide chemical and physical stability.[3] Moreover, TiO_2 shows high reactivity and can be used as a redox catalyst, although its reactivity is limited by the fast electron–hole pair recombination and the low efficiency of photogenerated electrons.[4,5] However, TiO_2 has a wide band gap of between 3.02 eV (rutile) and 3.23 eV (anatase),[6] which means that it can only absorb the UV range of sunlight with wavelengths smaller than 400 nm, constituting only 2–3% of the total sunlight spectrum.[7] To address this issue, the TiO_2 surface can be doped with transition metals like Fe, Co, Ni, or Pd.[8] While the use of transition metals increases reactivity, it is often non-economical and expensive. Additionally, cation-doped TiO_2 exhibits poor photostability.[7]

Alternatively, modifying TiO_2 to utilize visible light and enhance its photocatalytic activity can be achieved through the synthesis of nanocomposites with various carbonaceous materials. This approach has been shown to be effective in several studies,[1,9–34] with graphene or graphene oxide being particularly promising. These materials offer a direct means of overcoming the low quantum availability and low adsorption capacity of pure TiO_2.[35]

Graphene, consisting of single graphite sheets, is a carbon nanomaterial.[36] Since its initial synthesis and analysis in 2004, research on graphene, graphene oxide (GO), and reduced graphene oxide (reduced GO) has proliferated rapidly.[37] GO can be easily prepared *via* graphite oxidation, and graphene can be obtained through the treatment of graphite with suitable solvents or functionalization.[36] Graphene is a two-dimensional sheet of covalently bonded carbon atoms, which is the smallest building block of graphite.[38] The hexagonal honeycomb structure of sp^2-hybridized carbon atoms in graphene results in unique properties such as remarkable elastic and intrinsic strength.[39] Consequently, graphene is renowned for its high thermic stability, specific surface area (2630 $m^2\ g^{-1}$), high Young's modulus values, and high room-temperature carrier mobility, up to 20 × 104 $cm^2\ V^{-1}\ s^{-1}$.[40–42] These exceptional properties of graphene contribute to its remarkable electronic conductivity. Additionally, the conduction and valence bands of graphene overlap slightly, making it a zero-band semiconductor,[43,44] which is ideal for photocatalytic reactions.

[a] *Department of Chemistry, University of Paderborn, Warburger Str. 100, 33098 Paderborn, Germany*
[b] *Department of Physics, University of Paderborn, Warburger Str. 100, 33098 Paderborn, Germany*
[c] *Institute of Organic Chemistry, Clausthal University of Technology, Leibnizstr. Str. 6, 38678 Clausthal-Zellerfeld, Germany. E-mail: rene.wilhelm@tu-clausthal.de*
† Electronic supplementary information (ESI) available: UV/vis analytical data. See DOI: https://doi.org/10.1039/d3cy00461a

The combination of TiO_2 and graphene oxide offers a promising method for synthesizing a new hybrid material.[45] Compared to pure graphene, which is only stable in solutions with additives and synthesized in small quantities using the scotch tape method, graphene oxide can be produced in high yields. We utilized two different methods to synthesize graphene oxide. The most widely used method was developed by Hummers *et al.* in 1958,[46] where the resulting product, Hum GO **1** (Scheme 1), is obtained in the presence of sulfuric acid and sodium nitrate, followed by the addition of potassium permanganate. The resulting material has a large number of hydroxyl, epoxide, and carboxyl groups on the surface. The second method, published by Murakami *et al.* in 2014,[47] synthesizes graphene oxide (edge-GO, GO **2**, Scheme 1) in the presence of sulfuric acid and nitric acid, resulting in predominantly selective edge-functionalized carboxyl groups. Both methods produce a more chemically active material that is readily available for functionalization. The oxide groups give graphene a polar character, making the chemical and physical properties more accessible, although this leads to graphene oxides providing a stable suspension in solution.[41,48] This is due to supramolecular interactions through π π stacking and hydrogen bonding.[49,50] Furthermore, it has been found that graphene oxide exhibits good adsorption capacities for organic materials.[49]

Both materials possess properties that make them suitable for combination with TiO_2 to create photocatalysts. This is a promising heterogeneous system that exhibits remarkable transparency, absorptivity, and conductivity.[51,52] While Hum GO **1** demonstrates higher redox activity due to its various oxide groups and defects, GO **2** has a defect-free sp^2 hybridized conjugated structure, resulting in greater conductivity. Both graphene oxides minimize the recombination of photogenerated electron–hole pairs of TiO_2,[49] which should lead to higher photocatalytic activity across the UV to visible light range of the solar spectrum.

In this study, we investigate the photocatalytic activity of various graphene oxide/TiO_2 (TiO_2–GOx%) hybrids, each synthesized using a different method. We compare their respective photocatalytic activities to identify any differences between thermally and non-thermally treated composites. We will assess the reactivity through the degradation of methyl orange (MO) and the photocatalytic reduction of benzaldehyde. Finally, we will employ density functional theory (DFT) calculations to identify the possible sources of enhanced photocatalytic activity in the graphene oxide/TiO_2 hybrids.

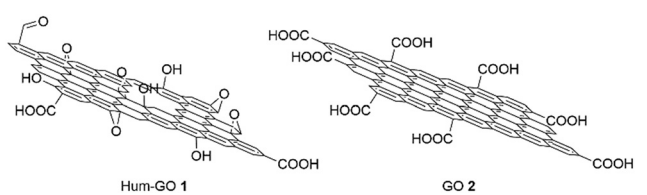

Scheme 1 Structure of the two different graphene oxides applied in this study.

2. Experimental section

2.1 Synthesis of GO 2 and composites

Edge-functionalized graphene oxide **2** was synthesized using a 3 : 1 mixture of 65% sulfuric acid and 95% nitric acid. The reaction mixture was sonicated for 3 h to obtain a homogeneous suspension, which was then stirred at 120 °C for 24 h. The resulting product was neutralized with sodium hydroxide solution and washed with deionized water using ultrafiltration (with a membrane filter of 0.2 μm FG, FLUOROPORETM) to obtain GO **2** in a high yield.[53]

The titanium oxide P25, 545S (P25 + 5 wt% SiO_2; specific surface area: 45 ± 10 m^2 g^{-1}) and 1580S (P25 + 15 wt% SiO_2; specific surface area: 80 ± 15 m^2 g^{-1}) were obtained from Evonik Industries.

In a typical reaction, either GO **2** or commercial Hum GO **1** was mixed with different types of TiO_2 (P25, 1580S, 545S) to form TiO_2–GOx% hybrids (at either 2% or 50% mass ratios of added graphene oxides). These hybrids were prepared by either grinding them together in an agate mortar (mechanical) or by exposing them to ultrasound for two minutes in a suspension of ethanol (neat). The resulting hybrids were then treated in a tube furnace under a nitrogen atmosphere with a heat rate of up to 400 °C to form the final composite.

2.2 Photocatalytic degradation of MO

As a general procedure, 10 mg of the composite material was added to an aqueous solution of methyl orange (12 ml, 0.4 mg mL^{-1}). To compare the photocatalytic activity of each measurement series, all samples were investigated in the absence of light by wrapping the reaction vessel completely with aluminum foil. The reaction mixture was stirred in the dark for 1 h to allow the absorption desorption equilibrium of MO to settle. After taking 3 mL for reference, measurements were taken in the presence of light. Each sample was irradiated with different sources of light, such as sunlight, a 20 W white LED made by uniTEC (400–800 nm), and 12 W of ultraviolet light (type Nu 6, 254 nm) from a distance of 3 cm for 30 min. After each irradiation, 3 mL of the sample was taken for analysis using UV/vis spectroscopy. The heterogeneous catalyst was removed using a PTFE syringe filter (0.2 μm).

2.3 Photocatalytic reduction

Generally, these composite materials were tested in the photocatalytic reduction of aldehyde under nitrogen atmosphere. Aldehyde (1 mmol, 1 eq.) was added to a suspension of TiO_2–*x*GOx% (10 mg) in 10 mL isopropyl alcohol and potassium hydroxide solution (0.1 mol L^{-1}). The mixture was stirred for 15 h under reflux. To investigate the influence of photocatalytic activity, the mixture was irradiated with different sources of light, like 12 W of ultraviolet light (type Nu-6, 254 nm or 366 nm), 3 W of ultraviolet LED (type LX 1206, 390–400 nm), 20 W white LED made by uniTEC

(400–800 nm) and 14 W blue LED made by Acelectronic (400–550 nm). After 15 h irradiation the reaction is ended by addition of 4 mL water. The crowed product was extracted with chloroform (3 × 10 mL), washed with sodium chloride solution (1 × 10 mL), water (2 × 10 mL) and dried over $MgSO_4$. Evaporation of the solvent affords the product in high yields.

Benzyl alcohol 3. Yield (100%) as colourless oil, ^{1}H-NMR (500 MHz, $CDCl_3$-d_1, TMS): δ [ppm] = 4.69 (s, 2 H, CH_2), 7.29–7.33 (m, 1 H, H4) 7.38 (d, J = 5.0 Hz, 4 H, H2, H3, H4, H5). ^{13}C-NMR (125 MHz, $CDCl_3$, TMS): δ [ppm] = 65.38 (CH_2), 127.08 (C-6, C-2), 127.71 (C-4), 128.64 (C-3, C-5), 141.05 (C-1).

4-Methoxybenzyl alcohol 4. Yield (13%) as yellow oil, ^{1}H-NMR (500 MHz, $CDCl_3$-d_1, TMS): δ [ppm] = 3.79 (s, 3 H, CH_3), 4.61 (s, 2 H, CH_2), 6.88 (d, J = 8.7 Hz, 2 H,), 7.28 (d, J = 8.7 Hz, 2 H). ^{13}C-NMR:[54].

4-Methylbenzyl alcohol 5. Yield (100%) as yellow oil, ^{1}H-NMR (500 MHz, $CDCl_3$-d_1, TMS): δ [ppm] = 2.36 (s, 2 H, CH_3), 4.65 (s, 2 H, CH_2), 7.18 (d, J = 7.8 Hz, 2 H), 7.26 (d, J = 8.0 Hz, 2 H). ^{13}C-NMR:[54].

2-Chlorobenzyl alcohol 6. Yield (52%) as yellow oil, ^{1}H-NMR (500 MHz, $CDCl_3$-d_1, TMS): δ [ppm] = 4.68 (s, 2 H, CH_2), 7.22–7.23 (m, 1 H), 7.24–7.25 (m, 1 H), 7.27–7.28 (m, 1 H), 7.37–7.38 (m, 1 H). ^{13}C-NMR:[54].

(Naphtalene-2-yl)methanol 7. Yield (46%) as orange solid, ^{1}H-NMR (500 MHz, $CDCl_3$-d_1, TMS): δ [ppm] = 4.87 (s, 2 H, CH_2), 7.47–7.50 (m, 3 H), 7.53–7.55 (m, 1 H), 7.78–7.80 (m, 1 H), 7.88 (d, J = 8.7 Hz, 1 H), 8.35 (s, 1 H). ^{13}C-NMR:[54].

Dibenzyledene acetone 8. Yield (38%) as colourless solid, ^{1}H-NMR (500 MHz, $CDCl_3$-d_1, TMS): δ [ppm] = 7.10 (d, J = 16.0 Hz, 2 H), 7.41–7.42 (m, 6 H), 7.61–7.63 (m, 4 H), 7.75 (d, J = 16.0 Hz, 2 H). ^{13}C-NMR:[55]. HRMS(ESI): found: m/z = 235.1124 ($[M + H]^+$); calculated: $C_{17}H_{14}O$ + H: 235.1122.

Bis-4-methoxybenzylidene acetone 9. Yield (15%) as colourless solid, ^{1}H-NMR (500 MHz, $CDCl_3$-d_1, TMS): δ [ppm] = 3.84 (s, 6 H, CH_3), 6.55 (d, J = 16.0 Hz, 2 H), 6.91–6.93 (m, 4 H), 7.54–7.56 (m, 4 H), 7.69 (d, J = 16.0 Hz, 2 H). ^{13}C-NMR:[56]. HRMS(ESI): found: m/z = 295.1335 ($[M + H]^+$); calculated: $C_{19}H_{18}O_3$ + H: 295.1336.

Diaryl ketone 9. Yield (36%) as orange solid, ^{1}H-NMR (500 MHz, $CDCl_3$-d_1, TMS): δ [ppm] = 7.23 (s, 6 H, 2H), 7.53–7.55 (m, 6 H), 7.83–7.85 (m, 8 H), 8.04 (s, 2 H). ^{13}C-NMR:[57]. HRMS(ESI): found: m/z = 335.1437 ($[M + H]^+$); calculated: $C_{19}H_{18}O_3$ + H: 335.1436.

2.4 Material characterization

Atomic force microscopy (AFM) from Veeco Dimension Icon by BRUKER was used to analyze the newly synthesized graphene oxide **2**. The utilization was carried out by NANOSCOPE ANALYSIS. Additional Raman spectroscopy and X-ray diffraction (XRD) were performed to confirm that the material was graphene oxide. The Raman spectrum was measured using an apparatus that combined an InVia spectroscope by RENISHAW with a DM2500 M microscope from LEICA MICROSYSTEMS.

The morphology of the newly synthesized heterogeneous catalyst was characterized using scanning electron microscopy (SEM) (Neon 40 from ZEISS). Energy dispersive X-ray spectroscopy (EDX) was also coupled to the SEM to enable the analysis of the catalyst's elements using an ultra-dry detector.

The degradation of MO was analyzed *via* UV-vis spectroscopy using Lambda 45 from PERKINELMER INSTRUMENTS. The measurements were conducted using SUPRASIL® quartz tubes (10 mm) from HELLMA®ANALYTICS.

2.5 Computational modelling: DFT calculations

The ORCA program[58] was utilized to perform all DFT calculations. Molecular geometry optimization and energy calculations were conducted using the B3LYP exchange–correlation functional[59,60] and def2-TZVP basis set.[61] To account for solvent (water) effects, the implicit solvation model (the conductor-like polarizable continuum model, CPCM)[62] was applied in all calculations. Additionally, we used the DFT-D3 van der Waals (vdW) correction[63] to account for long-range vdW interactions. The photocatalytic reductions of benzaldehyde were monitored by ^{1}H-NMR spectroscopy Avance 500 made by Bruker.

3. Results and discussion

3.1 Synthesis and characterization

3.1.1 Characterization of GO 2. The morphology was examined using SEM and AFM. Scheme 2a shows the surface of GO **2**. This structure is typically for graphene sheets and exhibits a uniform layer. A view of the EDX images shows increased oxygen enrichment in the fold and edge areas of the sample (Scheme 2b). This confirms the edge-functionalization of GO **2** with this method.[53]

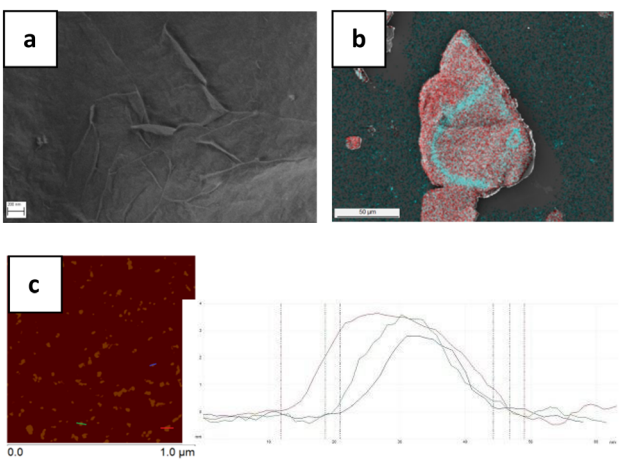

Scheme 2 a) SEM images of GO **2** (— 200 nm), EHK = 2.00 kV. b) EDX images of GO **2** with the element carbon (red) and oxygen (blue) measured on carbon pats (— 50 µm). c) AFM images (topography) measured on mica disks and the resulting depth profile of three nanosheets of GO **2**.

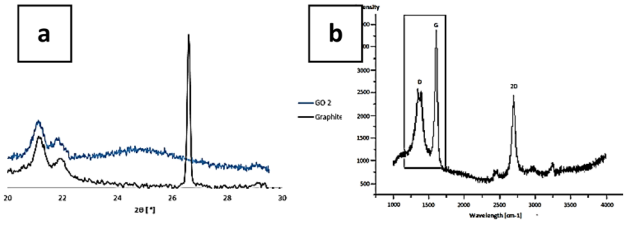

Scheme 3 a) XRD of GO **2** and graphite. b) Raman spectrum of GO **2**.

The XRD and Raman spectrum in Scheme 3 prove that it is clearly no longer graphite but GO **2**. Graphite shows a characteristic angle at $2\theta = 27°$ (Scheme 3a) in the XRD. This angle results in the layer-level distance of the crystal structure of graphite. A few layers mean a high degree of disorder and the peak at 27° becomes wider. Thus, a wide flat peak is characteristic for graphene.

Raman spectroscopy is used to analyze the ordered/disordered crystal structure.[3] As can be seen in Scheme 3b, the spectrum of GO **2** shows the typical G line (1600 cm^{-1}), resulting from the sp^2-system and the corresponding D line (1350 cm^{-1}), showing the sp^3-share in the system.[64] The relative intensity of the D band along with the G band results in the I_D/I_G relation. This parameter allowed for making a statement about the degree of defects in the graphene network. Based on the Tuinstra–Koenig model ($1/L_a$), whereby L_a includes the parameter I_D/I_G, there are 16 layers of GO **2**.[65] This confirmed the results of the AFM images (Scheme 2c).

3.1.2 Characterization of the composites TiO_2–GOx%. Table 1 shows all synthesized composites. To optimize the reaction conditions all samples were heat treated at 200, 300 and 400 °C in a tube furnace with a heat rate of 2 °C min^{-1}. All samples heat treated at 200 and 300 °C show no optical changes. Furthermore, the SEM shows any changes of the morphology. Compared to the samples which were converted at 400 °C, with a mass loss of 10% and a threefold increase in volume, the other samples showed no changes at lower temperatures. This is also consistent with the results of Jo *et al.* who in 2016 published that at least a temperature of 300 °C must be exceeded in order to combine TiO_2 with graphene oxide.[21] For this reason, non-thermally treated composites were compared with composites which were heat-treated at 400 °C to test in the photocatalytic activity.

To perform a complete characterization, pure P25 was first analyzed by SEM. As shown in Scheme 4 the nanoparticle of pure P25 shows a fine porous material. The particle has a spherical, close-packed structure.

The newly produced composite **18** exhibits a much larger graphenic layer before heat treatment (Scheme 5a and b). The 545S particles are evenly distributed and form agglomerates.

After heat treatment, the new material is more voluminous, lighter and highly electrostatic (Scheme 5c and d). The composite consists of several rounded graphene layers that form a large, oval honeycomb cluster (Scheme 5c). The magnification of the SEM image in Scheme 5d shows that the TiO_2 and SiO_2 particles are located in the edge area of the surface. In this area, a linkage between the hydrophilic oxygen groups of the titanium dioxide and the side functionalized GO could have taken place.

Like the 545S composite, which was not heat-treated, the GO **2**–1580S composite, which was mixed only at room temperature, also shows an angular, rougher graphene structure (Scheme 6a). The 1580S particles are distributed over the entire surface and form more agglomerates. The

Table 1 Summary of various synthesized composites heat treated at 400 °C

Nr.	Carbon [wt%]	P25 ratio [wt%]	545S (P25 + 5 wt% SiO_2)[33]	1580S (P25 + 15 wt% SiO_2)[33]
10	GO **2** [100]			
11		[100]		
12			[100]	
13				[100]
14	GO **2** [50]	[50]		
15	GO **2** [10]	[90]		
16	GO **2** [5]	[95]		
17	GO **2** [2]	[98]		
18	GO **2** [50][a]		[50]	
19	GO **2** [50]		[50]	
20	GO **2** [10]		[90]	
21	GO **2** [5]		[95]	
22	GO **2** [2]		[98]	
23	GO **2** [50][a]			[50]
24	GO **2** [50]			[50]
25	GO **2** [10]			[90]
26	GO **2** [5]			[95]
27	GO **2** [2]			[98]
28	Hum-GO [50]	[50]		
29	Hum-GO [2]	[98]		
30	Graphite [50]	[50]		
31	Graphite [10]	[90]		

[a] The heterogeneous catalyst was suspended in ethanol. After ultrasonic for 15 min the solvent was removed.

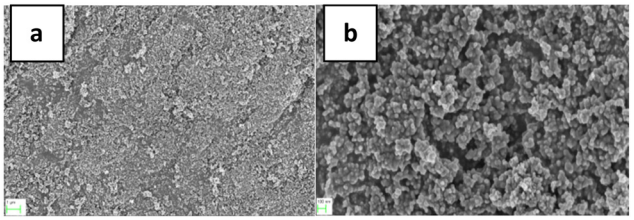

Scheme 4 a) SEM images of P25 (— 1 μm), EHK = 2.00 kV and b) (— 100 nm), EHK = 2.00 kV measured on carbon pad.

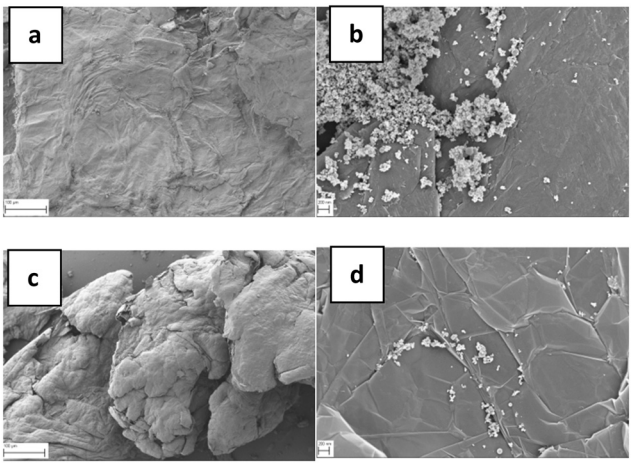

Scheme 5 a) SEM images of GO–545S$_{rt}$ (1 : 1) (— 100 μm) and b) (— 200 nm), c) SEM images of GO–545S$_{400°C}$ (1 : 1) **18** (— 100 μm) and d) (— 200 nm), EHK = 2.00 kV measured on carbon pad.

1580S particles have twice the specific surface area of the 545S particles with a size of 80 ± 15 m^2 g^{-1}. This could be the reason why, after the thermal treatment, the new composite is not a closed capsule but opened at the sides of the graphene clusters (Scheme 6b and c). The voluminous graphene clusters resemble a honeycomb. It can be assumed

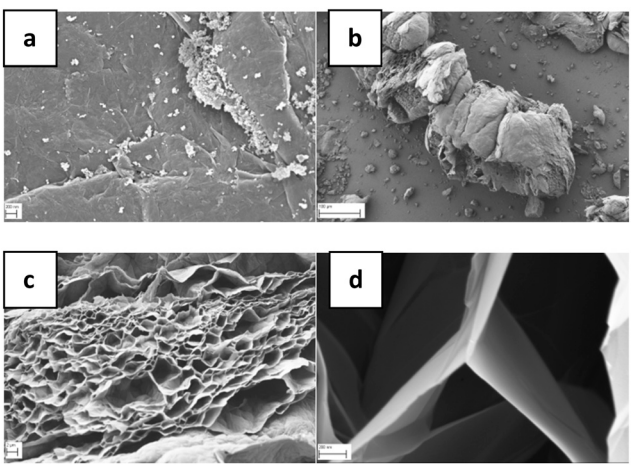

Scheme 6 a) SEM images of GO **2**–1580S$_{rt}$ (1 : 1) (— 200 nm) and b) SEM images of GO **2**–1580S$_{400°C}$ (1 : 1) **23** (— 100 μm), c) (— 2 μm) and d) (— 200 nm), EHK = 2.00 kV measured on carbon pad.

Table 2 Summary of other composites produced under optimized conditions

No.	Carbon [wt%]	P25 ratio [wt%]	Temperature [°C]	Method
28	Hum-GO [50]	[50]	400	Mechanical
32	Hum-GO [2]	[98]	400	Mechanical
33	Hum-GO [2]	[98]	400	Neat
34	Hum-GO [50]	[50]	rt	Mechanical
35	Hum-GO [2]	[98]	rt	Mechanical
36	Hum-GO [2]	[98]	rt	Neat

that the 1580S particles have been deposited in the layer and this led to the opening of this structure. Based on the results of the oxidative degradation of MO, further composites were produced under optimized conditions (Table 2). These should lead to a complete characterization of the catalytic activity.

In summary, the SEM images, the measured loss of mass and the increase in volume of the thermally treated composites can be used to conclude a successful morphological change in the composites. A temperature of at least 300 °C is required for this. Whether mechanically or neatly synthesized, there is no difference after heat treatment. Next, the photocatalytic activity of the different materials was investigated.

3.2 Photocatalytic degradation of MO

The produced composites were investigated in the oxidative degradation of methyl orange. The redox-dependent decomposition of azo dyes offers a fast way to determine the catalytic activity of new catalysts.[66–69] Pure titanium dioxide absorbs photons only in the UV-range at an absorption maximum of 350 nm.[70] Just like pure titanium dioxide, 545S and 1580S show only photocatalytic activity before and after thermal treatment by irradiation with UV light (see ESI,† Scheme S1). Accordingly, both the temperature and the silicon dioxide content in the material have no influence on the activity. The absorption range of around 465 nm results from the –N═N– azo compound of MO. The band at 270 nm results from the aromatic rings of MO. Both behave reciprocally when completely degraded. Compared to GO **2**, the MO aromatics are excited in the presence of 545S and 1580S at the same exposure time. At the same time, pure GO **2** shows no catalytic activity (see ESI,† Scheme S2). Measurement with 5 mg of GO **2** confirms that no scattering effects are involved in the non-existent activity of GO **2**. As a result, GO **2** acts as a sensitizer and not as a MO catalyst when the catalytic activity of the new composites is increased. The graphite/P25 **30** measurement was measured as a reference sample. It can be seen from the spectrum that decomposition takes place in the presence of graphite by irradiation with visible light.

In order to investigate the mass dependence, additional composites were produced in a ratio of 1 : 1. As can be seen in Scheme S3 in the ESI,† if the concentration of GO **2** is too high, the photocatalytic activity is inhibited. The too high

concentration of GO **2** leads to the fact that the P25 particles are completely shielded and can no longer act as a photocatalyst. In addition, the graphic nanoparticles **2** scatter the light quanta on the outside of the reaction vessel so that absorption of photons is not possible. Accordingly, a correct relationship between sensitizer and catalytically active species is important. A comparison of **14** and **17** also shows that, at a lower concentration of GO **2**, a decomposition of MO already takes place in the presence of visible light. This is proof that the combination of GO **2** with P25 increases the photocatalytic activity. The Scheme S4 in the ESI† shows the UV-vis spectra of the different GO **2**–545S. The composites **19** and **20** show the highest activity, whereby at **19** with a mass ratio of 50% GO **2**, a complete decomposition of MO takes place in the presence of LED. Composite **21** only decomposes in the UV range. At the same time, there is a high excitation of the aromatic rings of MO. The lower concentrated composites seem to lose activity. It can be seen in all spectra that the less GO **2** is used, the lower the photocatalytic activity of the composites. At the same time, it can be seen everywhere that the activity increases continuously from the dark reaction to the irradiation with UV. In all measurements, the dark reaction was taken as a reference. The UV-vis spectra of GO/1580S show the highest activity at a higher concentration of GO **2**. The composites with 2-wt% and 5-wt% GO **2** show no activity at all (Scheme S5, ESI†).

Consideration of the overall results for the decomposition of MO shows that the use of GO **2** has shifted the absorption behaviour into the visible range. Graphene oxide **2** acts as a sensitizer. Accordingly, even a small amount of energy is sufficient to excite the electrons in P25 and initiate a photocatalytic reaction. A too high concentration and a too low concentration of GO **2** turned out not to be productive. While many graphene oxides **2** lead to a complete inhibition of the reactivity, a too small amount is not sufficient to increase the activity.

3.3 Photocatalytic reduction of benzaldehyde

After the composites produced with 50-wt% and 10-wt% GO **2** proved to be the most effective during the decomposition of MO, they will be compared with those produced with Hum-GO **1** in the reduction of benzaldehyde. This raises the question to what extent the adsorption behavior and the electrical conductivity of both graphene oxides influence the photocatalytic activity of P25.

Scheme 7 schematically shows the photocatalytic sensitization of carbon-based materials with titanium dioxide. A comparison of GO **2** and Hum-GO **1** raises the question of which effects predominate. While GO **2** has a lower recombination rate of photogenerated electron–hole pairs due to the defect free conjugated π-system, Hum-GO **1** has a stronger link with titanium dioxide due to the higher functionalization rate. The high linking rate between Hum-GO **2** and titanium dioxide finally leads to a higher sensitization.[71] In order to evaluate the activity of the

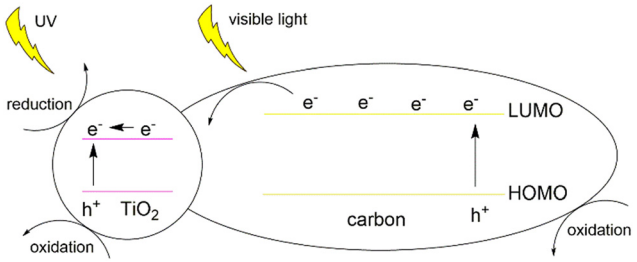

Scheme 7 General schema to illustrate the photocatalytic sensitization of carbon-based materials.

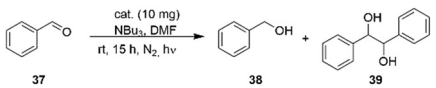

Scheme 8 Pinacol coupling and reduction of benzaldehyde **37**.

composites, the various catalysts produced were tested in the reduction of benzaldehyde (Scheme 8).

First, known reaction conditions were chosen.[72,73] The catalysts were investigated in the presence of NBu_3 as reductive quencher, using different light sources. The results are listed in Table 3. This shows that the absorption range of the new heterogeneous composites is within the visible range.

Since only traces of the product were obtained in a complete turnover, the reaction conditions were changed.[74] A solution of isopropanol and KOH with a concentration of 0.1 mol L^{-1} was used instead of NBu_3 as base. Furthermore, the reaction took place in the presence of 75 °C. In order to check the activity, the pure untreated materials were first examined (Table 4).

In contrast to the previous reaction, no pinacol coupling takes place using KOH (Scheme 9).

Furthermore, it could be observed that each material leads to a reduction of benzaldehyde to benzyl alcohol. Besides, a cross coupling takes place in some cases. The use of isopropanol causes an aldol reaction in the presence of aldehydes. Under a redox-active photocatalysis, an oxidation of isopropanol to acetone takes place. The acetone formed then reacts with benzaldehyde to form the aldol product. In 2018, Dhar *et al.* published that graphitic composites catalyze aldol condensation between aldehydes and acetone.[75] The working group used $MnFe_2O_4$/graphitic carbon nitride (g-C_3N_4) as catalytic species. In the absence of a base and at 70 °C, yields of up to 92% were achieved. The composites act as Lewis acid catalysts. In contrast to Dhar *et al.*, the aim of this work is to investigate the exact activity of the different materials produced. Furthermore, the reaction conditions of the light influence will be investigated.

A look at the results from Table 4 shows that the reaction also takes place without a photocatalyst. However, it can be seen that a light dependence can be observed with both base and the heterogeneous carbonaceous material. It is also clear that selectivity only takes place under certain conditions. Pure benzyl alcohol is formed only in the presence of higher

Table 3 Influence of irradiation wavelength on reduction of benzaldehyde

Entry	Catalyst	Light source	Product	NMR-ratio
1	GO/1580S (50%) **24**	White LED (400–700 nm)	HB, B	0.13
2	GO/1580S (50%) **24**	UV (366 nm)	n.r	n.r
3	GO/1580S (10%) **25**	White LED (400–700 nm)	HB, B	0.10
4	GO **2**	Near UV (390–400 nm)	HB, B	0.18
5	GO/P25 (50%) **14**	White LED (400–700 nm)	HB, B	0.03

B = benzaldehyde; BA = benzyl alcohol; HB = hydrobenzoin, n.r = no reaction, product/educt = NMR-ratio.

Table 4 Characterization and optimization of reactivity

Entry	Catalyst	Light source	Product	Yield
1	GO **2**	Near UV (390–400 nm)	BA	79%
2	545S	Near UV (390–400 nm)	BA	97%
3	1580S	Near UV (390–400 nm)	BA	100%
4	P25	Near UV (390–400 nm)	BA	93%
5	—	Near UV (390–400 nm)	BA	88%
6	—	UV (254 nm)	BA	43%
7	—	Blue LED (450–500 nm)	BA	54%
8	—	White LED (400–700 nm)	BA	14%
9[a]	—	White LED (400–700 nm)	BA	1%
			DBA	12%
10[b]	—	White LED (400–700 nm)	BA	13%
			DBA	38%
11[c]	—	White LED (400–700 nm)	n.r	—
12	—	—	BA	37%
13[a]	—	—	BA	1%
			DBA	17%

B = benzaldehyde; BA = benzyl alcohol; DBA = dibenzylideneacetone; n.r = no reaction. [a] Room temperature. [b] No inert gas. [c] Without base.

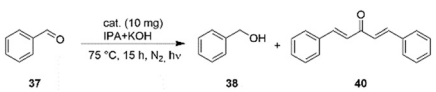

Scheme 9 Cross-coupling and reduction of benzaldehyde **37**.

temperatures, while DBA is preferably formed at room temperature and in the presence of oxygen. This confirms that the isopropanol present must first be oxidized in order to then further react in an aldol. The presence of oxygen promotes the base-catalyzed oxidation of isopropanol to acetone.

In another series of experiments, the light dependence of Hum-GO **1** was compared with GO **2** and P25 (Table 5). It turned out that in the presence of Hum-GO **1**, only DBA **40** is selectively formed. It can therefore be assumed that pure Hum-GO **1** is not photocatalytically active, whereas GO **2** and P25 show a high photocatalytic activity in which only benzyl alcohol **38** is selectively formed.

Table 5 Reactivity and light dependence in the heterogeneous reduction of benzaldehyde **37**

Entry	Catalyst	White LED (400–700 nm)	Near UV (390–400 nm)	UV (254 nm)
1	Hum-GO **1**	DBA (18%)	DBA (7%)	DBA (16%)
2	GO **2**	BA (81%)	BA (79%)	n.r
3	P25	BA (84%)	BA (93%)	BA (70%)

B = benzaldehyde; BA = benzyl alcohol; DBA = dibenzylideneacetone; n.r = no reaction.

In order to investigate the activity of Hum-GO **1** more closely, additional control reactions were performed. Table 6 clearly shows that the acidic character of Hum-GO **1** has a significant influence on the catalysis. Since all reactions were carried out under inert gas, the oxidation to benzoic acid **41** takes place exclusively in the presence of **1**. The control reaction confirms that Hum-GO **1** as a redox-active catalyst can have both reducing and oxidizing effects. By varying the reaction conditions, the course of the catalyst can be selectively controlled.

Since Hum-GO **1** itself is not photocatalytically active, a further screening was performed to investigate the photocatalytic activity of all differently produced composites based on Hum-GO **1** (Table 7). From the result it becomes clear that all composites have their absorption maximum at 400 nm. The reactivity decreases in the presence of low and high wavelength light. It can also be seen that thermally treated composites selectively reduce to benzyl alcohol **38** while with composites **34**–**36** also the formation of DBA could be observed.

The more P25 is present in the composites, the higher the reduction product. If, on the other hand, the proportion of Hum-GO **1** in the new materials is higher, the aldol-product is preferred. The thermally treated composites supply only the reduction product. Conversely, this means that the active species in the formation of the aldol-product are the hydrophilic groups of Hum-GO **1**. Thermal treatment of the composites again loses the acidic character of Hum-GO **1**.

Table 6 Control reaction for the activity of Hum-GO **1**

Entry	Condition	Yield BA **38**	Yield DBA **40**	Yield BAc **41**
1	Daylight	7%	12%	—
2	White LED, 36 h	4%	29%	—
3	rt	0.1%	5%	—
4	Cat. (20 mg)	—	—	5%
5	Cat. (5 mg)	8%	26%	—
6	Without base	—	—	10%
7	Without base, cat. (50 mg)	—	—	19%
8	NEt_3 as base	—	—	3%

B = benzaldehyde; BA = benzyl alcohol; DBA = dibenzylideneacetone; BAc = benzoic acid; n.r = no reaction.

Table 7 Influence of the used synthetic method of the new composites

Catalyst	White LED (400–700 nm)	Near UV (390–400 nm)	UV (254 nm)	Daylight
Hum-GO/P25 (50 wt%) **28** (mech., 400 °C)	BA (91%)	BA (99%)	BA (34%)	BA (71%)
Hum-GO/P25 (2 wt%) **32** (mech., 400 °C)	BA (98%)	BA (88%)	BA (58%)	BA (12%)
Hum-GO/P25 (2 wt%) **33** (neat, 400 °C)	BA (34%)	BA (100%)	BA (82%)	BA (89%)
Hum-GO/P25 (50 wt%) **34** (mech., rt)	DBA (40%) BA (9%)	DBA (28%), BA (28%)	n.r	n.r
Hum-GO/P25 (2 wt%) **35** (mech., rt)	BA (86%)	BA (94%)	DBA (22%), BA (59%)	n.r
Hum-GO/P25 (2 wt%) **36** (neat, rt)	BA (81%)	n.r	DBA (16%), BA (60%)	n.r

B = benzaldehyde; BA = benzyl alcohol; DBA = dibenzylideneacetone; BAc = benzoic acid; n.r = no reaction.

Furthermore, a direct comparison between LED and UV irradiation shows an ideal reciprocal behavior with respect to the yields.

Based on the results obtained, the following catalysis cycle is postulated in Scheme 10. The reaction mechanism consists of two cycles, one light-independent (**1**) and one light-dependent (**2**). The light-independent cycle **1** is a base-catalyzed cross coupling.[57] In a Meerwein–Ponndorf–Verley (MPV) reduction, aldehydes react with isopropanol (**A**) to a six-membered transition state (**B**). A secondary alcohol is essential for MVP reduction. It is only in this way that the necessary acetone and benzyl alcohol (**C**) can be formed *via* hydride transfer through a base such as KOH. Subsequent Claisen–Schmidt condensation with 2 eq. unreacted aldehyde leads to the Aldol product (**C**). Catalysis cycle **1** is a reversible reaction that takes place in both directions in a thermodynamic equilibrium. The fact that only the aldol product is selectively formed when Hum-GO **1** is added means that the acidic character of graphene oxides has a significant influence on the course of base catalyzed reactions.

If a photocatalytically active material is added to the system, another catalysis cycle takes place, the light-dependent cycle **2**. An aldehyde is adsorbed on the surface of the heterogeneous catalyst by means of π–π interaction or hydrogen bridge bonding (**D**). The electrons in the catalyst are then excited by absorption of light quanta. The graphic material acts both as a sensitizer and as an electron transporter (**E**). In the last catalytic step, a single electron transfer (SET) takes place. The carbonyl compound to the alcohol is reduced and at the same time an oxidation from the secondary alcohol to the carbonyl compound takes place. The photocatalytic redox reaction results in oxidation, reduction and recovery of the heterogeneous catalyst (**F**). Consideration of Table 8 also provides information on the reaction kinetics. While the C–C coupling product is preferably formed after 1 h, the reduction product is selectively formed after 15 h. As a result, the kinetically controlled product (cycle **1**) is formed in the presence of heterogeneous catalysts. If light with a suitable wavelength is added to the system, the thermodynamically more stable product is formed (cycle **2**).

To investigate the extent of the photocatalytic system, further control reactions with different analogues were performed under the general synthesis conditions (Table 9). It can be seen that the choice of substituents has a significant influence on the reactivity and selectivity of the reaction. Substituents with a strong +I-effect increase the reactivity of the light-dependent catalysis cycle (**2**) (entry 2). Hydroxyl groups in *para*-position have a deactivating effect, so that the −I-effect leads to an inhibition of the reaction. In the presence of substituents acting as electron donors, both catalysis cycles take place (entry 3). Halogens and methyl groups selectively lead to the reduction product (entry 4, 5). Furthermore, it becomes apparent that the position of the substituents has only a weak influence on the selectivity.

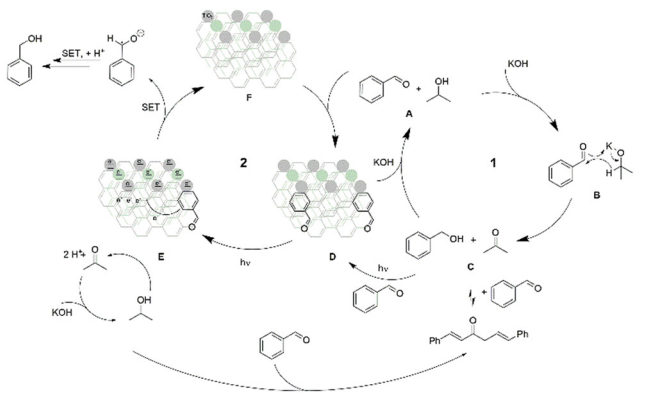

Scheme 10 Photocatalytic reaction cycle using the newly produced composites.

Table 8 Control reaction for the analysis of the catalysis cycle

Catalyst	White LED (400–700 nm), 15 h	White LED (400–700 nm), 1 h	Darkness
Hum-GO/P25 (2 wt%) **32**	BA (98%)	DBA (38%) BA (88%)	—
Hum-GO **2**	DBA (18%)	—	—
Hum-GO/P25 (50 wt%) **34**	DBA (40%) BA (9%)	—	—
—	—	—	BA (37%)
—[a]	—	—	DBA (17%) BA (1%)
—[b]	—	—	DBA (38%) BA (13%)

B = benzaldehyde; BA = benzyl alcohol; DBA = dibenzylideneacetone; – = not performed. [a] Room temperature. [b] Without inert gas.

Table 9 Scope of light-dependent photocatalytic reaction using different carbonyl derivatives

Entry	Aldehyde	Aldol-product	Reduction-product
1	Benzaldehyde **37**	26%	8%
2	4-Hydroxy benzaldehyde **41**	n.r	n.r
3	4-Methoxy benzaldehyde **42**	15%	13%
4	4-Methyl benzaldehyde **43**	—	100%
5	3-Chloro benzaldehyde **44**	—	52%
6	2-Naphtalenecarboxaldehyde **45**	36%	46%
7	Benzophenone **46**	—	1%

Reaction condition: 75 °C, 15 h, N_2, Hum-GO/P25 (50 wt%) **34** (5 mg), IPA + KOH, white LED. — = not performed; n.r = no reaction.

Ultimately, only mesomeric and inductive effects determine the course of the process. If the substituent is too bulky again, no reaction can take place due to steric effects.

3.4 DFT calculations

To elucidate the origins of the enhanced photocatalytic activity, the geometries and electronic structures of TiO_2/graphene oxide (GO) nanocomposites were modeled by means of DFT calculations. To model the TiO_2 nanoclusters, we used the structural model $(TiO_2)_{15}$, which we built following the procedure outlined in our previous work.[76] For GO, we employed the Lerf–Klinowski-type model (as shown in Scheme 11a), which was successfully used for DFT modeling of functionalization with porphyrins.[77]

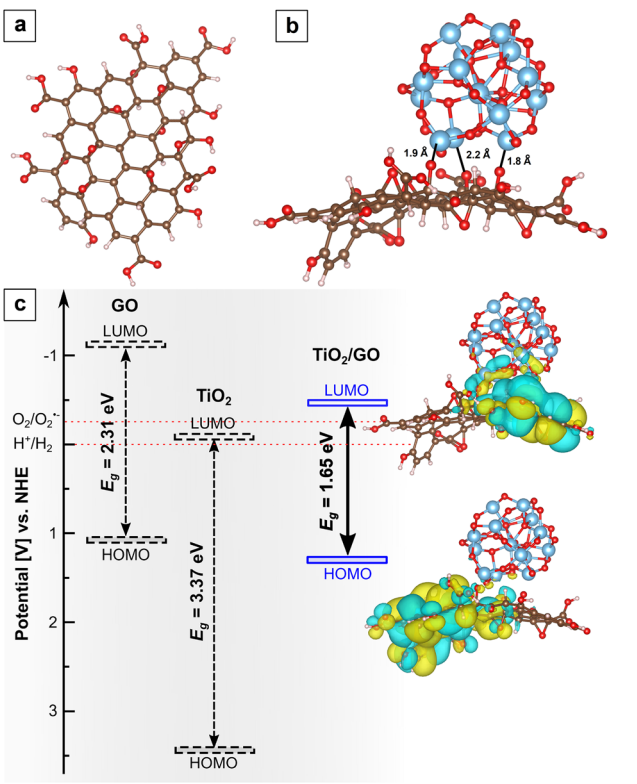

Scheme 11 a) DFT optimized structure of the Lerf–Klinowski-type GO model.[69] b) DFT optimized structure of the TiO_2/GO composite. The interfacial Ti–O_{GO} chemical bonds are indicated by solid black line. c) The calculated HOMO–LUMO gap of the composite (solid lines) compared to those of GO and $(TiO_2)_{15}$ before contact (dashed lines). The positions of frontier molecular orbitals (HOMO and LUMO) are plotted *versus* the normal hydrogen electrode (NHE). Isosurface plots of the HOMO and LUMO orbitals of the composite are shown on the right.

The DFT-optimized TiO_2/GO composites were found to be most stable (*i.e.*, exhibiting lowest energies) when the oxygens in GO form chemical bonds with the outer titanium ions of the $(TiO_2)_{15}$ surface. An example stable TiO_2/GO configuration is shown in Scheme 11b. It features three bridging Ti–O_{GO} bonds, with the bond lengths ranging from 1.8 to 2.2 Å. The formation of strong interfacial metal–oxygen bonds, as reported in GO composites with TiO_2 and other metal oxides,[78–80] is known to result in robust and thermally stable composites.

Subsequently, the binding strength between the materials was assessed by calculating the binding energies (ΔE_b) of the TiO_2/GO complex, by subtracting the total energies of TiO_2 and GO from the total energy of the TiO_2/GO complex ($\Delta E_b = E(TiO_2/GO) - E(TiO_2) - E(GO)$). The strongly negative ΔE_b values indicated that the formation of the composite is energetically favorable, with a value of −3.17 eV obtained for the structure depicted in Scheme 11b, suggesting high thermodynamic stability of the composite.

Next, electronic structure calculations were performed to assess the photocatalytic activity of the composite (see Scheme 11c). The calculated positions of the highest-occupied molecular orbital (HOMO) and lowest unoccupied molecular orbital (LUMO) of the TiO_2/GO composite were 1.27 V and −0.37 V, respectively, relative to the normal hydrogen electrode (NHE). These results reveal that the introduction of the electronic states of GO resulted in a significant decrease in the HOMO–LUMO gap, E_g, of the composite compared to that of the pure TiO_2 nanocluster. For the considered DFT-optimized TiO_2/GO structure, the calculated energy gap was 1.65 eV (compared to 3.37 eV for the bare nanocluster), indicating a shift of the photoresponsiveness into the visible range, consistent with the experimental observations.

Finally, while the exact HOMO and LUMO energies of TiO_2/GO are expected to depend on a specific binding scenario, Scheme 11c shows that the LUMO position of the composite can potentially be shifted to the range that favors the generation of superoxide radical ($O_2^{\bullet-}$) from dissolved oxygen molecules. For the considered structural model of TiO_2/GO, the

calculated LUMO position (−0.37 V) is more negative than that of $O_2/O_2^{\bullet-}$ (−0.28 V).[81] Superoxide radical is known to play a central role in the photocatalytic decomposition of organic pollutants, including MO.[82] Thus, our results provide a rationale for the observed photodegradation of MO by the TiO_2/GO hybrids in the presence of visible light.

4. Conclusions

The use of heterogeneous photocatalysts based on graphene oxide offers an inexpensive, easily producible and green alternative to conventional metal-based photocatalysts. The synthesis of the composites plays an important role in the reactivity of the catalysts. Titanium dioxide as the photocatalytically active part is combined with graphene oxide as the electron sink or donor. The more oxidative groups there are, the greater the acidic character of the material and thus the influence as redox material in the catalysis cycle used; in this case it strongly influences the base-catalyzed part of the reaction. If the material is thermally treated, the acid content decreases and the new composite can be used as electron donor or sink in a photocatalytic reaction. In addition, it was successfully demonstrated that side functionalized GO **2** and pure titanium dioxides are photocatalytically active. A combination of the two leads to a shift of the activity into the visible range. This is not the case with the use of Hum-GO **1**. A higher photocatalytic activity can only be noted after thermal treatment. Accordingly, the position of the oxidative groups on the graphic surface also has a considerable influence on the catalytic activity.

Conflicts of interest

There are no conflicts to declare.

Acknowledgements

Deutsche Forschungsgemeinschaft (DFG), project numbers WI2147/17 and SCHM1361/25 is acknowledged for financial support. The authors thank the Paderborn Center for Parallel Computing (PC^2) and the Höchstleistungs–Rechenzentrum Stuttgart (HLRS) for grants of high-performance computer time. We thank Sabuhi Badalov for helpful discussions and the Evonik Industries AG for the donation of 1580S and 545S.

References

1 M.-Q. Yang, N. Zhang, M. Pagliaro and Y.-J. Xu, *Chem. Soc. Rev.*, 2014, **43**, 8240–8254.
2 D. Parviz, S. Das, H. S. T. Ahmed, F. Irin, S. Bhattacharia and M. J. Green, *ACS Nano*, 2012, **6**, 8857–8867.
3 G. Jiang, Z. Lin, C. Chen, L. Zhu, Q. Chang, N. Wang, W. Wei and H. Tang, *Carbon*, 2011, **49**, 2693–2701.
4 X.-Y. Zhang, H.-P. Li, X.-L. Cui and Y. Lin, *J. Mater. Chem.*, 2010, **20**, 2801–2806.
5 V. Stengl, J. Henych, P. Vomáčka and M. Slušná, *Photochem. Photobiol.*, 2013, **89**, 1038–1046.
6 M. Grätzel and F. P. Rotzinger, *Chem. Phys. Lett.*, 1985, **118**, 474–477.
7 S. K. Warkhade, G. S. Gaikwad, S. P. Zodape, U. Pratap, A. V. Maldhure and A. V. Wankhade, *Mater. Sci. Semicond. Process.*, 2017, **63**, 18–24.
8 K. Jiahui, L. Chunhua, W. Jian, C. Yukai and X. Zhongzi, *Chem. Rev.*, 2017, **117**, 1445–1514.
9 H. Sun and S. Wang, *Energy Fuels*, 2014, **28**, 22–36.
10 I. V. Lightcap and P. V. Kamat, *Acc. Chem. Res.*, 2013, **46**, 2235–2243.
11 A. Adán-Más and D. Wei, *Nanomaterials*, 2013, **3**, 325–356.
12 J. Low, S. Cao, J. Yu and S. Wageh, *Chem. Commun.*, 2014, **50**, 10768–10777.
13 M. Dahl, Y. Liu and Y. Yin, *Chem. Rev.*, 2014, **114**, 9853–9889.
14 S. Iijima, *Nature*, 1991, **354**, 56–58.
15 L. Forró, J. P. Salvetat, J. M. Bonard, R. Basca, N. H. Thomson, S. Garaj, L. Thien-Nga, R. Gaál, A. Kulik, B. Ruzicka, L. Degiori, A. Bachtold, C. Schönberger, S. Pekker and K. Hernadi, in *Science and Application of Nanotubes*, ed. D. Tomanek and R. J. Enbody, Kluwer-Plenum, New York, 2000, p. 297.
16 P. M. Ajayan, *Chem. Rev.*, 1999, **99**, 1787–1799.
17 M. S. Dresselhaus, G. Dresselhaus and M. Pimenta, *Eur. Phys. J. D*, 1999, **9**, 69–75.
18 M. S. Dresselhaus, G. Dresselhaus, K. Sugihara, I. L. Spain and H. A. Goldberg, *Graphite Fibers and Filaments*, Springer, Berlin-Heidelberg, 1988.
19 S. Iijima, *J. Cryst. Growth*, 1980, **50**, 675–683.
20 D. Ugarte, *Nature*, 1992, **359**, 707–710.
21 H.-H. Chun and W.-K. Jo, *Appl. Catal., B*, 2016, **180**, 740–750.
22 I.-C. Chen, L. H. Chen, X.-R. Ye, C. Daraio, S. Jin, C. A. Orme, A. Quist and R. Lal, *Appl. Phys. Lett.*, 2006, **88**, 153102.
23 M. Ge and K. Sattler, *Chem. Phys. Lett.*, 1994, **220**, 192–196.
24 S. Iijima, M. Yudasaka, R. Yamada, S. Bandow, K. Suenaga, F. Kokai and K. Takahashi, *Chem. Phys. Lett.*, 1999, **309**, 165–170.
25 J. Miyawaki, M. Yudasak, H. Imai, H. Yorimitsu, H. Isobe, E. Nakamura and S. Iijima, *Adv. Mater.*, 2006, **18**, 1010–1014.
26 J. Shen, J. Li, Q. Chen, T. Luo, W. Yu and Y. Qian, *Carbon*, 2006, **44**, 190–193.
27 L. Song, L. Chi, L. Sun, C. Jin, L. Liu, W. Ma, D. Liu, X. Zhao, S. Luo, Z. Zhang, Y. Xiang, J. Zhou, W. Zhou, Y. Ding, Z. Wang and S. Xie, *Adv. Mater.*, 2006, **18**, 1817–1821.
28 A. Krüger, *Adv. Mater.*, 2008, **20**, 2445–2449.
29 S. K. Fatima, A. S. Ceesay, M. S. Khan, R. Sarwar, M. Bilal, J. Uddin, A. Ul-Hamid, A. Khan, N. Riaz and A. Al-Harrasi, *ACS Omega*, 2023, **8**, 3007–3016.
30 Y. Sun, J. Sun, M. Que, L. Chen, F. Chen and B. Tang, *New J. Chem.*, 2022, **46**, 12139–12147.
31 A. Hardiansyah, W. J. Budiman, N. Yudasari, I. T. Kida and A. Wibowo, *ACS Omega*, 2021, **6**, 32166–32177.
32 S. Sarkar, A. Raghavan, A. Giri and S. Ghosh, *ChemistrySelect*, 2021, **6**, 10957–10964.
33 K. Wang, L. Liang, Y. Zheng, H. Li, X. Niu, D. Zhang and H. Fan, *New J. Chem.*, 2021, **45**, 16168–16178.

34 M. Maiti, M. Sarkar and D. Liu, *Catal. Sci. Technol.*, 2020, **10**, 2797–2809.
35 C. Xu, Y. Yuan, R. Yuan and X. Fu, *RSC Adv.*, 2013, **3**, 18002–18008.
36 H.-X. Wang, Q. Wang, K.-G. Zhou and H.-L. Zhang, *Small*, 2013, **9**, 1266–1283.
37 K. S. Novoselov, A. K. Geim, S. V. Morozov, D. Jiang, Y. Zhang, S. V. Dubonos, I. V. Grigorieva and A. A. Firsov, *Science*, 2004, **306**, 666–669.
38 G. Bottari, M. Á. Herranz, L. Wibmer, M. Volland, L. Rodríguez-Pérez, D. M. Guldi, A. Hirsch, N. Martín, F. D'Souza and T. Torres, *Chem. Soc. Rev.*, 2017, **46**, 4464–4500.
39 C. Lee, X. Wei, J. W. Kysar and J. Hone, *Science*, 2008, **321**, 385.
40 K. I. Bolotin, K. J. Sikes, Z. Jiang, M. Klima, G. Fudenberg, J. Hone, P. Kim and H. L. Stormer, *Solid State Commun.*, 2008, **146**, 351–355.
41 U. Khan, A. O'Neill, M. Lotya, S. De and J. N. Coleman, *Small*, 2010, **6**, 864–871.
42 S. Park and R. S. Ruoff, *Nat. Nanotechnol.*, 2009, **4**, 217–224.
43 M. Bacon, S. J. Bradley and T. Nann, *Part. Part. Syst. Charact.*, 2014, **31**, 415–428.
44 A. K. Geim, *Science*, 2009, **324**, 1530–1534.
45 K. Ullah, S. Ye, Z. Lei, K.-Y. Cho and W.-C. Oh, *Catal. Sci. Technol.*, 2015, **5**, 184–198.
46 W. S. Hummers and R. E. Offeman, *J. Am. Chem. Soc.*, 1958, **80**, 1339.
47 R. Sekiya, Y. Uemura, H. Murakami and T. Haino, *Angew. Chem., Int. Ed.*, 2014, **53**, 5619–5623.
48 L. Li, H. Duan, X. Wang and C. Luo, *New J. Chem.*, 2014, **38**, 6008–6016.
49 W. Xiao, P. Zhao, S. Deng and N. Zhang, *New J. Chem.*, 2015, **39**, 3719–3727.
50 Y. H. Ng, I. V. Lightcap, K. Goodwin, M. Matsumura and P. V. Kamat, *J. Phys. Chem. Lett.*, 2010, **1**, 2222–2227.
51 H. Zhang, X. Lv, Y. Li, Y. Wang and J. Li, *ACS Nano*, 2010, **4**, 380–386.
52 W.-J. Ong, L.-L. Tan, S.-P. Chai and S.-T. Yong, *Chem. Commun.*, 2015, **51**, 858–861.
53 A. Wolk, M. Rosenthal, S. Neuhaus, K. Huber, K. Brassat, J. K. N. Lindner, R. Grothe, G. Grundmeier, W. Bremser and R. Wilhelm, *Sci. Rep.*, 2018, **8**, 5843.
54 S. Sharma, D. Bhattacherjee and P. Das, *Adv. Synth. Catal.*, 2018, **360**, 2131–2137.
55 K. Farrell, H. Müller-Bunz and M. Albrecht, *Organometallics*, 2015, **34**, 5723–5733.
56 J. George, J. Sharma, R. Joshi and R. T. Pardasani, *Res. Chem. Intermed.*, 2015, **41**, 5681–5689.
57 N. Satrawala, K. N. Sharma, L. C. Matsinha, L. Maqeda, S. Siangwata, G. S. Smith and R. K. Joshi, *Tetrahedron Lett.*, 2017, **58**, 2761–2764.
58 F. Neese, *Wiley Interdiscip. Rev.: Comput. Mol. Sci.*, 2022, **12**, e1606.
59 A. D. Becke, *Phys. Rev. A: At., Mol., Opt. Phys.*, 1988, **38**, 3098–3100.
60 C. Lee, W. Yang and R. G. Parr, *Phys. Rev. B: Condens. Matter Mater. Phys.*, 1988, **37**, 785789.
61 F. Weigend and R. Ahlrichs, *Phys. Chem. Chem. Phys.*, 2005, **7**, 3297–3305.
62 V. Barone and M. Cossi, *J. Phys. Chem. A*, 1998, **102**, 1995–2001.
63 S. Grimme, J. Antony, S. Ehrlich and H. Krieg, *J. Chem. Phys.*, 2010, **132**, 154104.
64 S. Claramunt, A. Varea, D. López-Díaz, M. M. Velázquez, A. Cornet and A. Cirera, *J. Phys. Chem. C*, 2015, **119**, 10123–10129.
65 F. Tuinstra and J. L. Koenig, *J. Chem. Phys.*, 1970, **53**, 1126–1130.
66 F. Chen, H. Liu, S. Bagwasi, X. Shen and J. Zhang, *J. Photochem. Photobiol., A*, 2010, **215**, 76–80.
67 J. Liu, Q. Zhang, J. Yang, H. Ma, M. O. Tade, S. Wang and J. Liu, *Chem. Commun.*, 2014, **50**, 13971–13974.
68 Y. Zhang, Y. Wang, R. Xie, H. Huang, M. K. H. Leung, J. Li and D. Y. C. Leung, *Environ. Sci. Technol.*, 2022, **56**, 16582–16601.
69 R. Girija, S. Mary, G. Balakrishnan, S. M. Mariappan, M. S. Hamdy and M. Shkir, *ChemistrySelect*, 2022, **7**, e202103614.
70 A. Zyoud, N. Zaatar, I. Saadeddin, M. H. Helal, G. Campet, M. Hakim, D. Park and H. S. Hilal, *Solid State Sci.*, 2011, **13**, 1268–1275.
71 S. Wang, I. S. Cole and Q. Li, *Chem. Commun.*, 2016, **52**, 9208–9211.
72 M. Nakajima, E. Fava, S. Loescher, Z. Jiang and M. Rueping, *Angew. Chem., Int. Ed.*, 2015, **54**, 8828–8832.
73 S. Zhu, A. Das, L. Bui, H. Zhou, D. P. Curran and M. Rueping, *J. Am. Chem. Soc.*, 2013, **135**, 1823–1829.
74 Y. Wang, P. Ren, X. Gu, X. Wen, Y. Wang, X. Guo, E. R. Waclawik, H. Zhu and Z. Zheng, *Green Chem.*, 2016, **18**, 1482–1487.
75 B. Bhuyan, D. J. Koiri, M. Devi and S. S. Dhar, *Mater. Lett.*, 2018, **218**, 99–102.
76 S. V. Badalov, R. Wilhelm and W. G. Schmidt, *J. Comput. Chem.*, 2020, **41**, 1921–1930.
77 A. Siklitskaya, E. Gacka, D. Larowska, M. Mazurkiewicz-Pawlicka, A. Malolepszy, L. Stobiński, B. Marciniak, A. Lewandowska-Andrałojć and A. Kubas, *Sci. Rep.*, 2021, **11**, 1–14.
78 S. Umrao, S. Abraham, F. Theil, S. Pandey, V. Ciobota, P. K. Shukla, C. J. Rupp, S. Chakraborty, R. Ahuja, J. Popp, B. Dietzek and A. Srivastava, *RSC Adv.*, 2014, **4**, 59890–59901.
79 J. M. Polfus, O. M. Løvvik, P. M. Rørvik and R. Bredesen, *J. Eur. Ceram. Soc.*, 2016, **36**, 719–724.
80 J. M. Polfus and K. Jayasayee, *Carbon*, 2019, **152**, 497–502.
81 T. Berger, D. Monllor-Satoca, M. Jankulovska, T. Lana-Villarreal and R. Gomez, *ChemPhysChem*, 2012, **13**, 2824–2875.
82 W. Li, D. Li, Y. Lin, P. Wang, W. Chen, X. Fu and Y. Shao, *J. Phys. Chem. C*, 2012, **116**, 3552–3560.

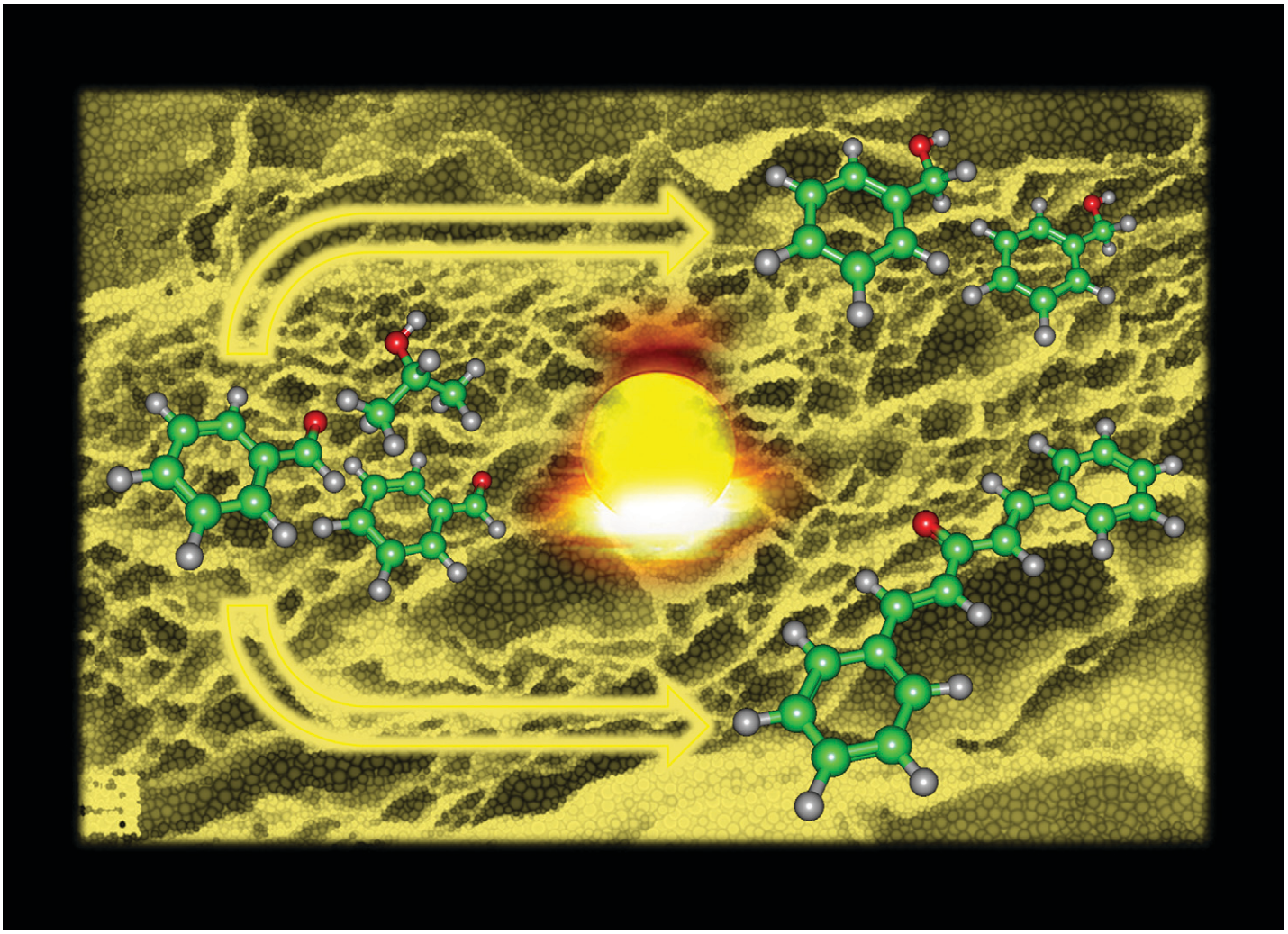

Showcasing research from Professor René Wilhelm's laboratory, Institute of Organic Chemistry, Clausthal University of Technology, Clausthal-Zellerfeld, Germany.

Synthesis of new graphene oxide/TiO_2 and TiO_2/SiO_2 nanocomposites and their evaluation as photocatalysts

The synthesis of graphene oxide - P-25 and TiO_2/SiO_2 hybrid materials, as well as their photocatalytic behaviour is discussed. Different synthetic routes to these composites were studied. Two different types of graphene oxide were used: edge-functionalized graphene oxide (edge-GO) and graphene oxide produced using the Hummers method (Hum-GO). The photocatalytic activity of the different nanocomposites was analysed by studying the degradation of methyl orange (MO) and the photocatalytic reduction of benzaldehyde. The different graphene oxide types, TiO_2 materials, and synthetic routes had an impact on the photocatalytic activity and selectivity.

As featured in:

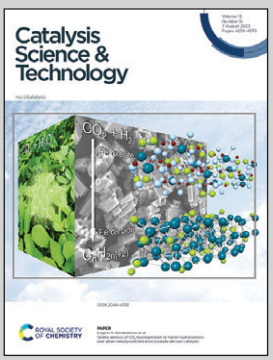

See René Wilhelm *et al.*, *Catal. Sci. Technol.*, 2023, **13**, 4367.

ROYAL SOCIETY OF CHEMISTRY

rsc.li/catalysis

Registered charity number: 207890